Chapter 4

Photochemical Production of H_2 from Water with Visible Light as Catalyzed by Hybrid Catalysts of CdS Attached to Microporous and Mesoporous Silicas

Abstract

Microporous and mesoporous silicas are combined with nanoparticulate CdS particles to form hybrid photocatalysts that produce H_2 from water/ethanol solutions under visible light irradiation. Catalyst structures are characterized by XRD and SEM. All hybrid materials are active photocatalysts for water splitting, and the order of photoactivity is found to be zeolite-Y > SBA-15 > zeolite L. Silica cavity size, which determines CdS particle size, and photocatalytic activity are found to be correlated. Photocatalytic activity is seen to decrease under acidic or basic conditions with an associated negative ionic strength effect. In addition, XPS analysis indicates loss of Cd^{2+} ion from the silicate supports occurs during the course of the photochemical reaction with apparent retention of bound CdS.

Introduction

Photocatalytic water splitting into H_2 and O_2 is an area of great interest due to the potential of hydrogen gas as a clean-energy fuel source. Since the initial work of Fujishima and Honda,[1] many different metal oxide semiconductors and metal sulfides have been reported to be active for water splitting. While initial efforts involved large bandgap (E_g > 3.0 eV) semiconductors that could only utilize UV light, recent efforts have focused on using visible light as the energy source,[2-21] as the ultimate goal is to use solar energy to produce hydrogen fuel. While the overall redox potential of the reaction

$$H_2O + h\nu \rightarrow H_2 + ½\ O_2 \qquad (4.1)$$

is only -1.23 eV (1000 nm) at pH 7, the crucial reaction for hydrogen production is believed to be the initial one-electron transfer to H^+ ion

$$H^+ + e^-_{aq} \rightleftharpoons H^*_{aq}\ , \qquad (4.2)$$

where E_H = -2.5V at pH 7, which falls energetically within the visible region of light.

CdS is an n-type semiconductor with a bandgap energy of 2.4 eV; it also well known to have photocatalytic activity for H_2 production under visible light irradiation,[22-25] although sacrificial electron donors are often used to prevent the photocorrosion of CdS in the presence of O_2. In an effort to increase photocatalytic yield, CdS is often combined with other semiconductors such as TiO_2/CdS,[26] ZnO/CdS, ZnS/CdS,[27,28] $K_4Nb_6O_{17}$/CdS,[29] and $K_2Ti_4O_9$/CdS composites.[30,31] An alternative approach is to couple CdS with mesoporous materials to form hybrid or composite photocatalysts.

There are several advantages that microporous and mesoporous materials afford as hosts for semiconductor particles. For example, the pore sizes of the host support material control the resulting particle size of the supported semiconductor. Decreasing

particle size has a known beneficial effect on catalyst efficiency.[32-35] Furthermore, encapsulation into a porous structure should provide some protection against surface-mediated reactions that corrode the catalyst, as exposed surface area will be limited. In addition, a major factor that limits the photocatalytic efficiency of CdS, or any other photocatalyst, is electron-hole recombination. Photogenerated electrons in CdS are can move into the attached porous molecule, while the holes remain behind, providing charge separation and increased photocatalytic efficiency.

Since silicates are good candidates for such a host molecule, we have explored several the use of Zeolite-Y, Zeolite-L, and SBA-15. Zeolite-Y is a microporous aluminosilicate with a supercage structure, having a pore diameter of 0.74 nm and a cavity diameter of 1.2 nm, while Zeolite-L is a microporous aluminosilicate with connected SiO_4 and AlO_4 tetrahedra that give rise to one-dimensional channels (aperture size 0.71 nm) arranged in a hexagonal structure. Zeolite-L has been shown to have excellent catalytic properties, such as isobutene dehydrogenation and oxidative cyclization.[36] It also has been used to make dye composites with optical antenna properties.[37] SBA-15, which was first reported by Zhao et al.,[38] is a highly ordered mesoporous silica with two-dimensional hexagonal symmetry, extremely high surface area, and controllable pore size ranging from 3 to 30 nm.

Experimental

Instrumentation

UV-vis diffuse reflectance spectra were recorded on a Shimadzu UV-2101PC with an integrating sphere attachment (Shimadzu ISR-260), using Ba_2SO_4 powder as an internal reference. BET surface area measurements were performed on a Micromeritics Gemini 2360 Analyzer. Diffuse infrared fourier transform (DRIFT) spectra were acquired using a Bio-Rad FTS-45 spectrometer with a liquid N_2-cooled MCT detector. Spectra were collected at 8 cm^{-1} resolution using a Spectra-Tech Collector diffuse-reflectance accessory. The solid samples were held in the sample cup of a Spectra-Tech high temperature environmental chamber (HTEC) that could be resistively heated to 1000 K (±1 K), and the chamber evacuated to 10 μTorr.

SEM images were taken on a LEO 1550VP FESEM. XRD spectra were recorded on a Phillips X'Pert PRO X-ray diffraction system. XPS experiments were performed in an M-probe surface spectrometer (VG Instruments) using monochromatic Al K_α X-rays (1486.6 eV).

Photolysis experiments were performed by using the collimated output of a high-pressure Hg-Xe arc lamp as a light source. The light beam was passed through an IR filter, a focusing lens and a 400 nm cutoff filter before reaching the reactor. The reactor was cooled by a fan to keep it at room temperature. Since it is well known that colloidal CdS suspensions undergo photocorrosion[39-41] and photocatalytic dissolution[42-46] under oxic conditions, the H_2 production experiments were carried out under an argon atmosphere. All photolysis reactors were purged with Ar gas for 30 minutes in order to eliminate O_2.

H_2 was measured using gas chromatography (HP 5890 Series II) with a thermal conductivity detector (TCD). Due to similar conductivity values for He and H_2, nitrogen was used as a carrier gas. The separations were achieved with a molecular sieve column (30 m × 0.32 mm × 12.00 μm). The gas chromatograph oven temperature was 30 ^{o}C, as this was found to be the best temperature for spatial resolution between Ar (reactor purge gas) and H_2. Calibration curves were linear over a broad range of H_2 concentrations.

Unless otherwise specified, the catalyst loading was 0.2g, the reaction solution was 50 mL of 50:50 ethanol/water, and the lamp power was 500 W. Aliquots of the reactor's headspace gas (total headspace volume = 100 mL) were syringed out in 50μL volumes through a rubber septum. Samples were taken every 8-12 hours, and several samples were taken at each time point to ensure accuracy.

Synthesis of CdS/Zeolite Composites

Cadmium sulfide was synthesized within the pore spaces of aluminosilicate zeolites[47-54] by the direct reaction of sorbed Cd^{2+} with aqueous S^{2-}. Commercially available Zeolite-Y (Si/Al=6) (Strem Chemicals) was used as received. The following procedure was used for synthesis of all CdS/zeolite samples. One gram of zeolite was added to a 50 mL solution of ethanol containing 1×10^{-2} M cadmium acetate. The covered solution was stirred for 48 hours. A 50 mL solution of ethanol containing $1x10^{-2}$ M sodium sulfide was prepared in a Vacuum Atmospheres glove box. The sodium sulfide solution was slowly added to the cadmium acetate solution while stirring, resulting in a yellow colored solution. The resulting solution was covered and stirred for 24 hours. The pH of this solution was between pH 6.0 and 6.5. The catalyst was then removed from solution by vacuum filtration, washed several times with ethanol, and dried

overnight in an oven at 100 ^{o}C. The yield from this procedure was always greater than 90%. The amounts of all materials were sometimes increased proportionally in order to generate larger amounts of catalyst (i.e., using twice as much zeolite, cadmium acetate, ethanol, etc.).

Synthesis of Zeolite-L

The synthesis and characterization of Zeolite-L has been reported by many authors.[36,55-58] Following procedures outlined in the literature, two different sizes of Zeolite-L were synthesized, one with a larger particle size (500-600 nm), and the other being much smaller (30-100 nm).

Large Zeolite-L

The desired elemental ratio of the synthesis mixture was $3K_2O$-$1Al_2O_3$-$10.7SiO_2$-$169.3H_2O$. In one flask, 3.175g KOH and 1.475g $Al(OH)_3$ were added to 6.225g H_2O, and the resulting solution was refluxed overnight in a mineral oil bath at 100 ^{o}C. The solution was initially cloudy but turned clear within 20 minutes. The second flask had 6.0g Aerosil OX50 silica in 22.77g H_2O. This solution was stirred, and placed in an ultrasound bath for 30 minutes to break up the silica particles, but was not refluxed. After the overnight reflux, the $Al(OH)_3$/KOH solution was slowly added to the silica solution, while stirring vigorously, in a Teflon reactor. The resulting solution became viscous and turned white. After 10 minutes of stirring, the solution was transferred to Teflon-lined tubes that were secured inside metal bomb casings. The metal bombs were put in an oven at 433K for 5 days. After 5 days, the brownish supernatant was removed, leaving behind a white precipitate, which was scooped out into a centrifuge tube. The precipitate was resuspended in hot water and centrifuged at 6000 rpm for 10 minutes.

The supernatant was decanted, and the product resuspended with shaking and vortexing. The centrifugation process was repeated 5-7 times until the pH of the supernatant became neutral. The resulting solid was dried at 100 ^{o}C in an oven overnight.

Small Zeolite-L

The desired elemental ratio of the synthesis mixture was $10K_2O$-$1Al_2O_3$-$20SiO_2$-$400H_2O$. Several failed attempts were made before finding a mixing ratio that worked. Initially, a solution containing 12.0g silica, 5.6g KOH, and 36.0g H_2O was used, but upon reflux this solution turned into a clear solid gel that stuck to the walls of the glass reaction vessel. Reducing the amount of KOH to 2.8g led to a similar result. It was determined that more water was needed to fully dissolve the silica. In one flask, 2.8g KOH and 1.56g $Al(OH)_3$ were added to 18g H_2O. In the second flask, 12.0g Aerosil OX50 silica and 8.4g KOH were added to 54g H_2O. Both solutions were refluxed overnight, and then mixed together and placed in the Teflon-lined pressure vessels as described earlier in the large Zeolite-L procedure. The bombs were placed in a rotating oven (rotating at 40 rpm) at 433K for 24 hours. The resulting precipitate was washed as described earlier, and the centrifugation process was repeated 8-11 times until the pH of the supernatant stopped dropping from 1 consecutive wash to another, giving an end point of pH 9. Unlike the large Zeolite-L sample, this sample was hard to resuspend, as the solid was more of a semiclear gel than a clump of solid powder. Thus the washing process was likely not as effective, which is why it took more attempts to lower the pH. The resulting solid was dried at 100 ^{o}C in an oven overnight.

Synthesis of SBA-15

SBA-15 was synthesized following procedures in the literature.[59,60] 4.0g of the surfactant P123 triblock copolymer was added to a solution containing 30g of H_2O and 120g of 2M HCl. The solution was stirred for 1 hour at room temperature, and then 8g of tetraethyl orthosilicate (TEOS) was added. The solution was stirred for 20 hours at 308K, and then aged at 353K for 5 hours. The solution was filtered, and the resulting solid product was washed with ethanol four times, then dried in an oven at 353K for a few hours. Some of the powder was then calcined at 773K for 5 hours.

Results and Discussion

Before creating the CdS/porous silica composites, it was first necessary to confirm that some of the starting silicas were synthesized correctly, specifically Zeolite-L and SBA-15 (Zeolite-Y was not synthesized and thus not analyzed). Figure 4.1 shows the XRD spectra of small vs. large Zeolite-L. As expected, there was increased line broadening in the small Zeolite-L sample, indicating smaller particle size. Unfortunately, XRD of SBA-15 was inconclusive. The characteristic peaks are all at a very low angle, and were not able to be seen. It was believed that the XRD instrument was not able to detect such low angle peaks. Figure 4.2 shows an SEM image of small Zeolite-L, which unfortunately does not look as clean as many of the SEM images reported in the literature for Zeolite-L. Figure 4.3 shows SEM images of synthesized SBA-15, which clearly show the tunnel-like structure of SBA-15. These images are similar to those found in the literature.[38]

The CdS/silica composites were analyzed by various techniques to gain insight into the structure and chemistry of the materials. Figure 4.4a shows the UV-vis diffuse reflectance spectra of the starting silicas and the CdS/silica composites, as well as commercial CdS. As expected, incorporation of CdS into the silica shifted the absorption edge into the visible. To calculate the bandgap energies, the spectra were converted into Tauc plots (figure 4.4b) by plotting $(\boldsymbol{F(R)}*E)^n$ vs. E, where $\boldsymbol{F(R)}$ is the Kubelka-Munk function (a transform of absorbance spectrum) and n = ½ for a direct bandgap semiconductor like CdS. The resulting bandgap energies are listed in table 4.1. For the synthesized compounds, the compound with the smallest cavity size (CdS/Zeolite-Y) has the smallest, or most red shifted, bandgap energy. The trend of increased cavity size vs.

increased bandgap energy continues across all samples. This result runs counter to the usual blue shift in wavelength with decreasing particle size. A possible explanation is that the absorption being measured is not from cavity-bound CdS, but rather surface CdS aggregates, and that CdS/Zeolite-Y has the largest size aggregates. Since we do not believe surface CdS is responsible for the majority of the photocatalytic activity, the UV-vis spectra may not provide a good indicator of which catalysts will perform best.

Surface areas were measured by BET, and are listed in table 4.2. In general, addition of CdS decreased available surface area. In the case of SBA-15, calcination increased surface area by removing the surfactant support molecules. Calcination resulted in a loss of approximately 25% of the sample's mass, and the surface area was increased by 50%. However, calcined CdS/SBA-15 showed no photocatalytic activity. It is likely that calcination removed the positively-charged surfactant triblock copolymers that served as substitution sites for Cd^{2+} ion,[60] thus preventing the incorporation of CdS particles into structure. Figure 4.5 shows the DRIFT spectra for uncalcined SBA-15 and the corresponding CdS/SBA-15 composite. There was no evidence of a peak for CdS, however this may just mean that the CdS was in an IR inactive form. Note that the hydrocarbon peaks at 2800 cm^{-1}, which are from the surfactant copolymer, were not present in calcined SBA-15.

Figure 4.6 shows DRIFT spectra comparing zeolites to the CdS/zeolite composites. In both CdS composites, a peak was detected that is assigned to nanosize CdS. In Zeolite-L peak location was 1570 cm^{-1}, in Zeolite-Y it was at 1585 cm^{-1}. The FTIR peak assigned to CdS is much sharper than that of commercial CdS powder, which

was also examined. This is evidence that at least some of the CdS particles are very small, likely on the order of nanometers.

Figure 4.7 shows hydrogen production for the various CdS/zeolite and CdS/SBA-15 materials. Zeolite-Y was the most photoactive (k = 6.6 μm H_2 hr^{-1}), followed by SBA-15 (k = 2.7 μm H_2 hr^{-1}), Zeolite-L large (k = 1.7 μm H_2 hr^{-1}), and Zeolite-L small (k = 1.3 μm H_2 hr^{-1}). As increased photocatalytic activity with decreasing particle size is a well-known phenomenon,[61,62] this would seem to indicate that the CdS nanoclusters are the smallest in Zeolite-Y. Indeed, the observed pattern of increasing photocatalytic activity correlates to the corresponding decrease in silica cavity size.

A variety of experiments were performed in an attempt to optimize hydrogen production. The effect of lamp power was explored, and as shown in figure 4.8, hydrogen production rate was linear over the range of lamp output power. Figure 4.9 shows the effect of ionic strength on hydrogen production. Increasing the ionic strength of the solution with sodium perchlorate decreased the amount of hydrogen produced. The thickness of the electrical double layer around the CdS/Zeolite-Y, which is given by the reciprocal of the Debye parameter κ (i.e., κ^{-1} in units of length), can be determined as follows:

$$\kappa \equiv \left(\frac{2\,F^2 \mu}{\varepsilon \varepsilon_0 RT} \right)^{0.5},$$

where ε is the dielectric constant of the solvent or mixed solvent system, ε_0 is the permittivity of free space (8.854×10^{-12} C^2 J^{-1} m^{-1}), μ is the ionic strength of the background electrolyte (mol m^{-3}), R is the gas constant (8.314 J mol^{-1} K^{-1}), T is temperature in units of K, and F is the Faraday constant (96,485 C mol^{-1}). With ε = 78.5

(X_{H2O} = 0.5) and ε = 24.3 (X_{EtOH} = 0.5), the thickness of the electrical double layer for an ionic strength of 1.0 mol m^{-3} (10^{-3} M) at T = 298 K gives κ^{-1} = 7.9 nm. For the concentrations of sodium perchlorate used in the ionic strength experiments (0.01, 0.1, and 0.5 M), and assuming a starting background electrolyte concentration of 10^{-3} M, the calculated thickness of the double layer is 2.37, 0.78, and 0.35 nm, respectively. Note that it is hard to know what the base background ionic strength is. The contribution from solvent should be minimal, but it is likely that ions (such as Cd^{2+}) leech out of the catalyst during the course of the experiment. It would appear that the electric double layer can be compressed to at least 2.37 nm with no adverse affect on reaction rate, but compression to ~1 nm leads to a noticeable drop-off in catalytic efficiency.

Figure 4.10 shows the effect of acid or base addition on hydrogen production. Both adding acid and base decreased photocatalytic activity. In several of the experiments where acid and base were added to the catalyst solution, there was no change pH. This is because the catalyst itself has some self-buffering capacity due to the presence of surface Si–OH and Al–OH groups. At the typical experimental pH (~9), the silanol groups will be deprotonated, and the aluminol groups will be protonated. Thus, there is capacity to absorb both H^+ and OH^- from solution. These experiments also increased ionic strength, but that effect alone can not account for the decreased photocatalysis rate. In the case of the base experiments, there is a steady drop off in reactivity despite constant pH. It is likely that at increased base concentration, there are less available surface protons that can participate in the formation of H_2. In the case of acid addition, there is a very sharp drop-off in both pH and reactivity when acid concentration was changed from 1×10^{-3} to 2.5×10^{-3} M. Somewhere in this range, it is

likely that the capacity for the silanol groups to absorb protons was reached. The excess protons then likely interfered with other surface groups, like S–H, shutting down the reaction.

During the course of the photoreaction, the reaction mixture is seen to turn from yellow to gray. Upon exposure to air, the yellow color is recovered within minutes. The gray color is likely the result of Cd^{2+} ions being photoreduced to Cd^{0} metal. Figure 4.11 provides a possible schematic for the cycling in cadmium oxidation states. To gain insight into the fate of the CdS during the photoreaction, the post-reaction catalyst was collected by filtration, washed, and examined by XPS. Figure 4.12 shows XPS data for the Cd $3d^{5/2}$ and $3d^{3/2}$ states in CdS/Zeolite-Y before and after photolysis. Two distinct forms of Cd are observed, and the ratio of the two changes after the photoreaction. The higher-energy peaks in each pairing (414.1 and 407.3 eV) are assigned to CdS, and the lower-energy peaks (413.3 and 406.5 eV) are assigned to Cd-substituted zeolite sites, which would have CdO character. Reference data indicates CdS to have a binding energy between 0.7 and 1.1 eV higher than CdO,[63] which is consistent with the 0.8 eV difference in peak positions. Using the Si and Al peaks to normalize the relative peak areas between the two samples (the overall Si and Al content should not change), it was found that there was a 21% loss of Cd that occurred during photolysis, but no net loss of sulfur (the XPS sulfur signal was too weak to perform individual peak assignment, only total area could be measured). The loss in intensity is seen as a reduction in the CdO peak, which can be explained as follows. It is likely that not all Cd substitution sites were accessible for formation of CdS, and thus remained in the zeolite matrix as Cd counterions. The Cd at these substitution sites could then leech out of the zeolite during

the 24-hour reaction period. Another possibility is that the Cd loss was actually from CdS particles that had been photocorroded, but that the sulfur atoms stayed behind.

Conclusions

Various microporous and mesoporous silicas were combined with nanosize CdS particles to produce catalysts that could produce H_2 gas from water/ethanol solutions using visible light. All compounds were active photocatalysts for water splitting, and the order of photoactivity was found to be Zeolite-Y > SBA-15 > Zeolite-L. Optimizing reaction conditions will be critical to achieving a high level of hydrogen production: pH, ionic strength, and water to alcohol ratio all have a marked effect on catalyst efficiency. Preventing loss of CdS during the course of the photoreaction is also paramount to creating a stable, long-term-use catalyst.

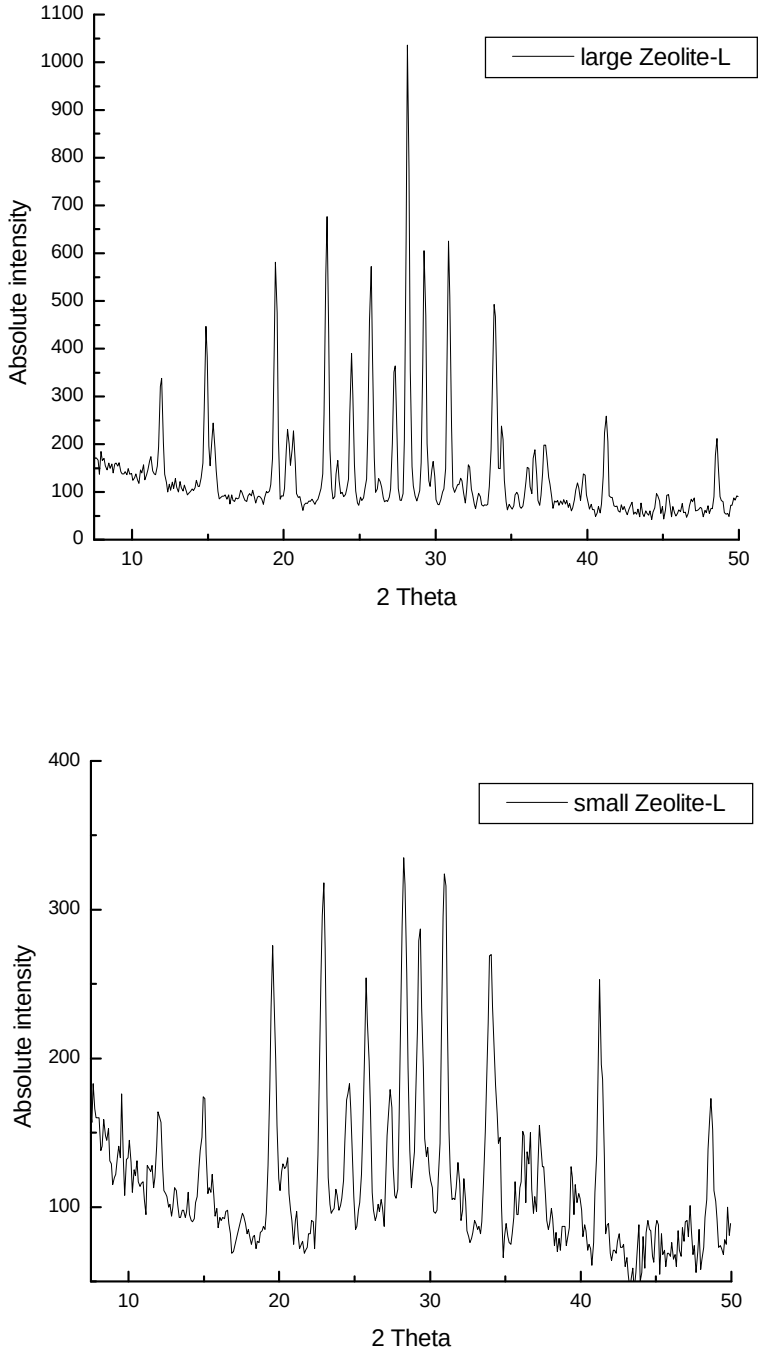

Figure 4.1. XRD of large Zeolite-L (top) and small Zeolite-L (bottom).

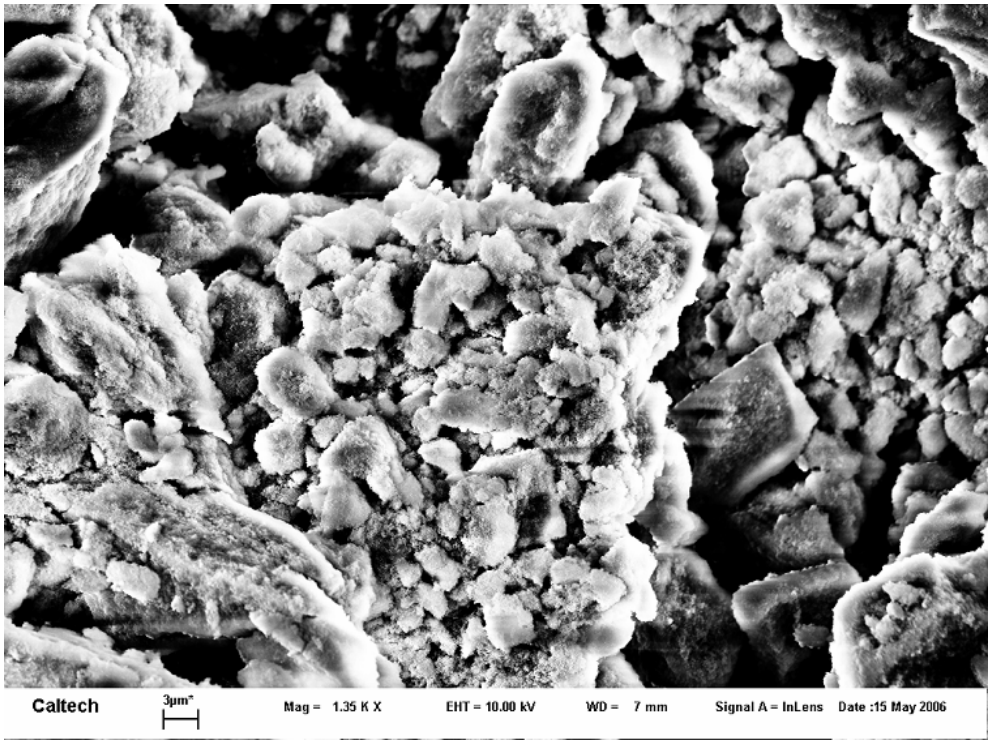

Figure 4.2. SEM image of small Zeolite-L. Scale is 3 μm.

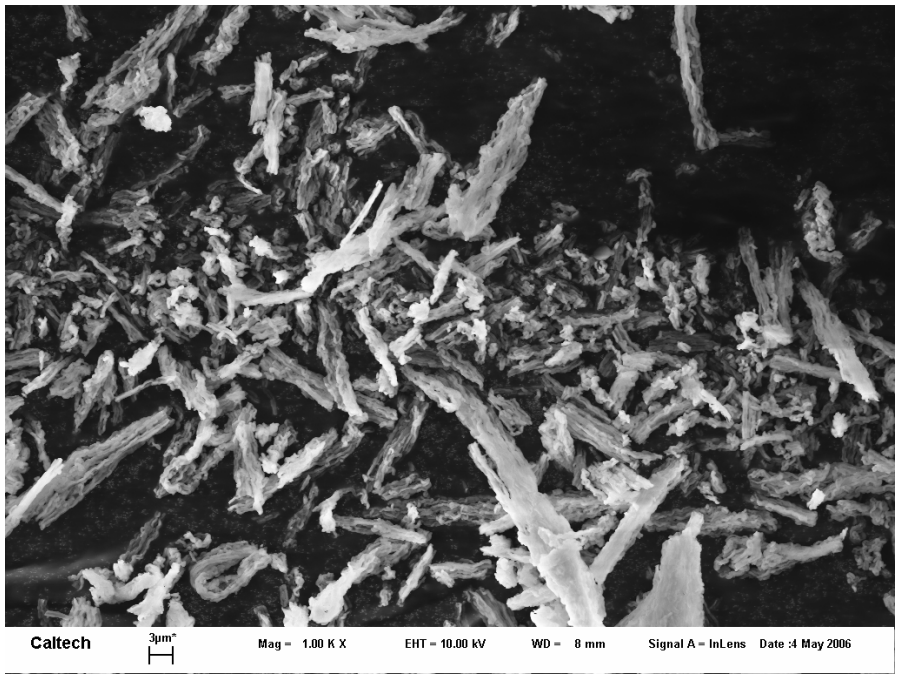

Figure 4.3. SEM images of calcined SBA-15 (scale is 3 mm for top image, 300 nm for bottom image).

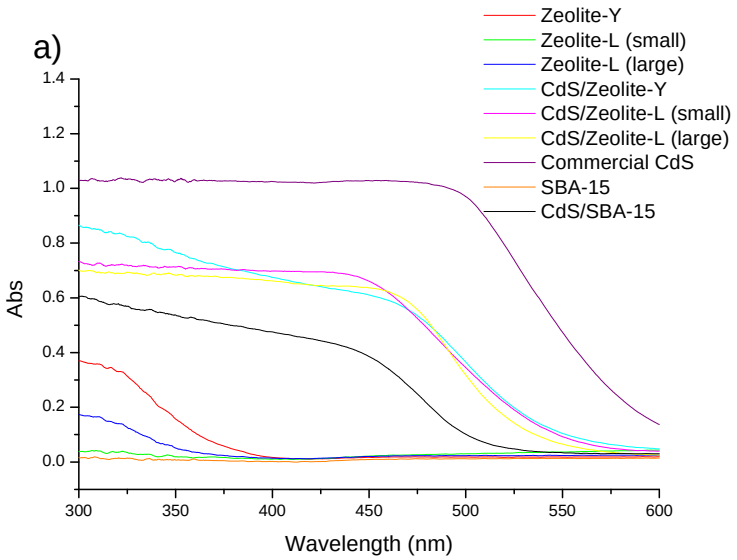

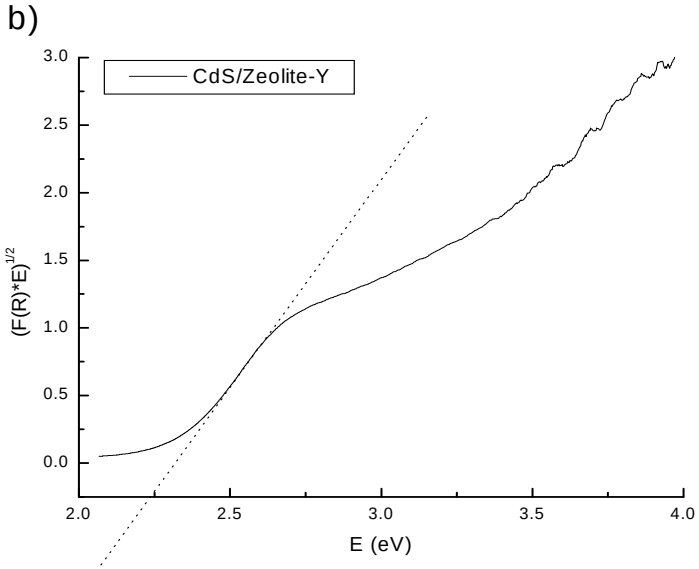

Figure 4.4. a) UV-vis diffuse reflectance spectra for the various starting silicas, CdS/silica composites, and commercial CdS. b) Tauc plot of CdS/Zeolite-Y, calculated from the UV-vis spectrum in figure 4.4 a).

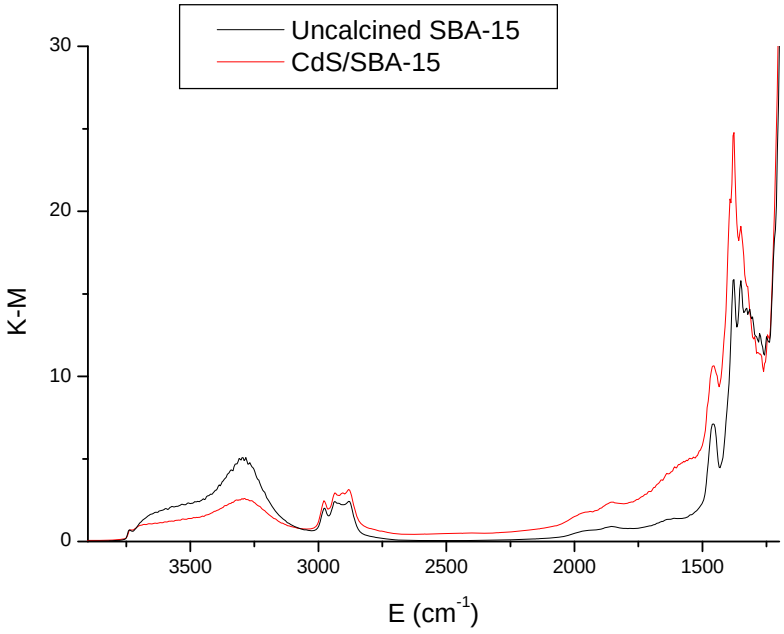

Figure 4.5. DRIFT spectra for uncalcined SBA-15 and the CdS/SBA-15 composite.

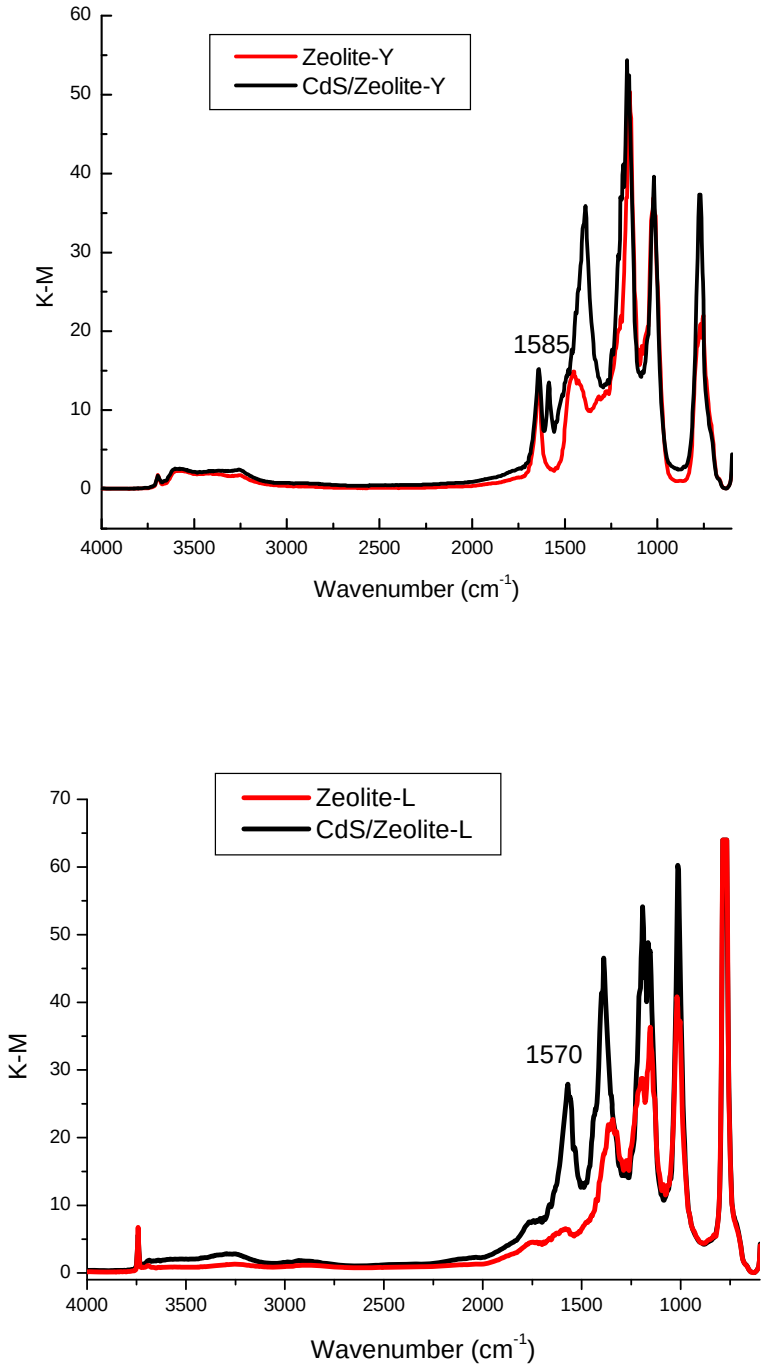

Figure 4.6. DRIFT spectra for Zeolite-Y and CdS/Zeolite-Y (top), and small Zeolite-L and CdS/Zeolite-L (bottom).

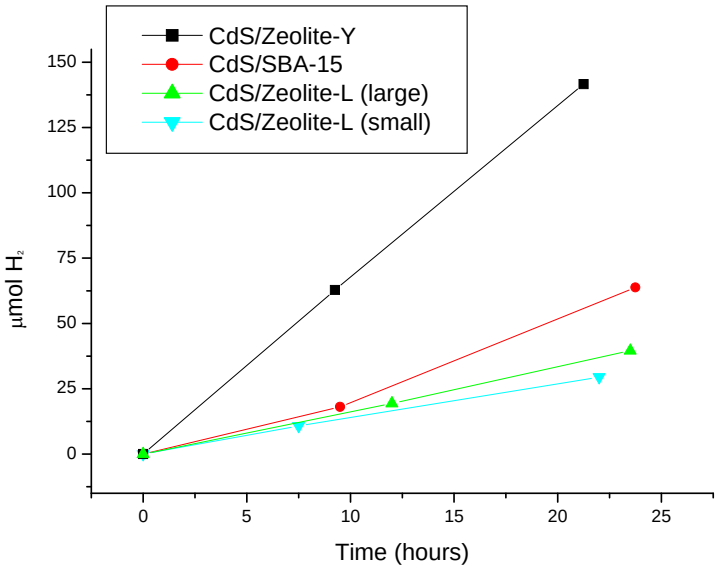

Figure 4.7. Hydrogen production for CdS/silica composites.

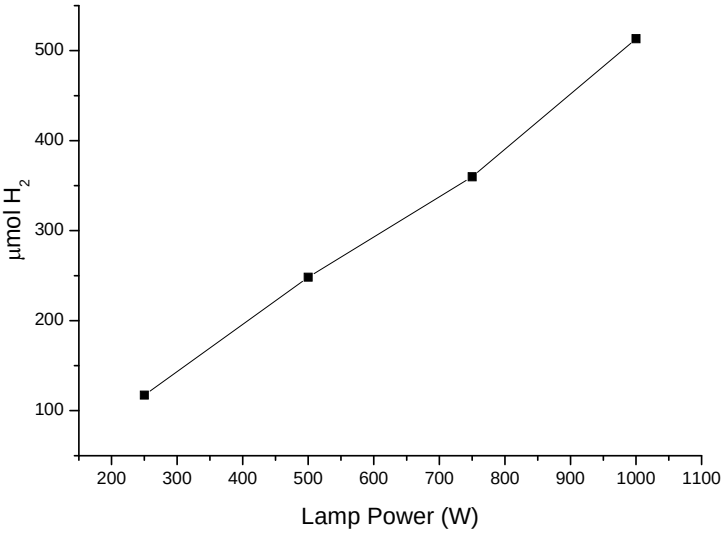

Figure 4.8. Light flux (lamp power as a surrogate for light intensity) vs. hydrogen production for CdS/Zeolite-Y.

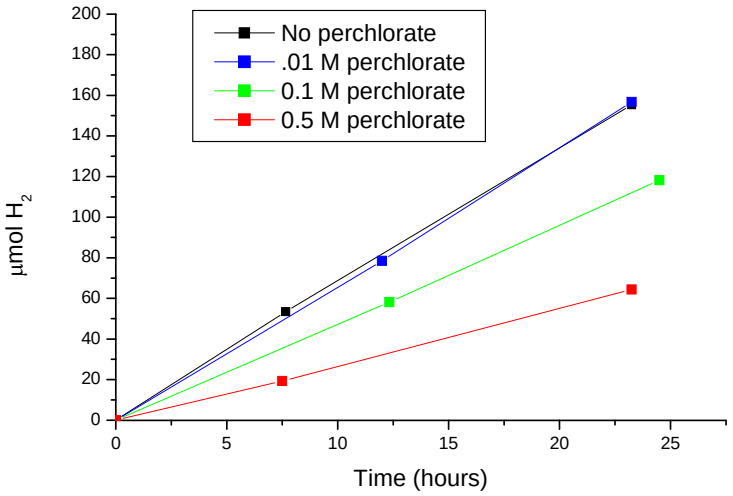

Figure 4.9. Ionic strength vs. hydrogen production for CdS/Zeolite-Y.

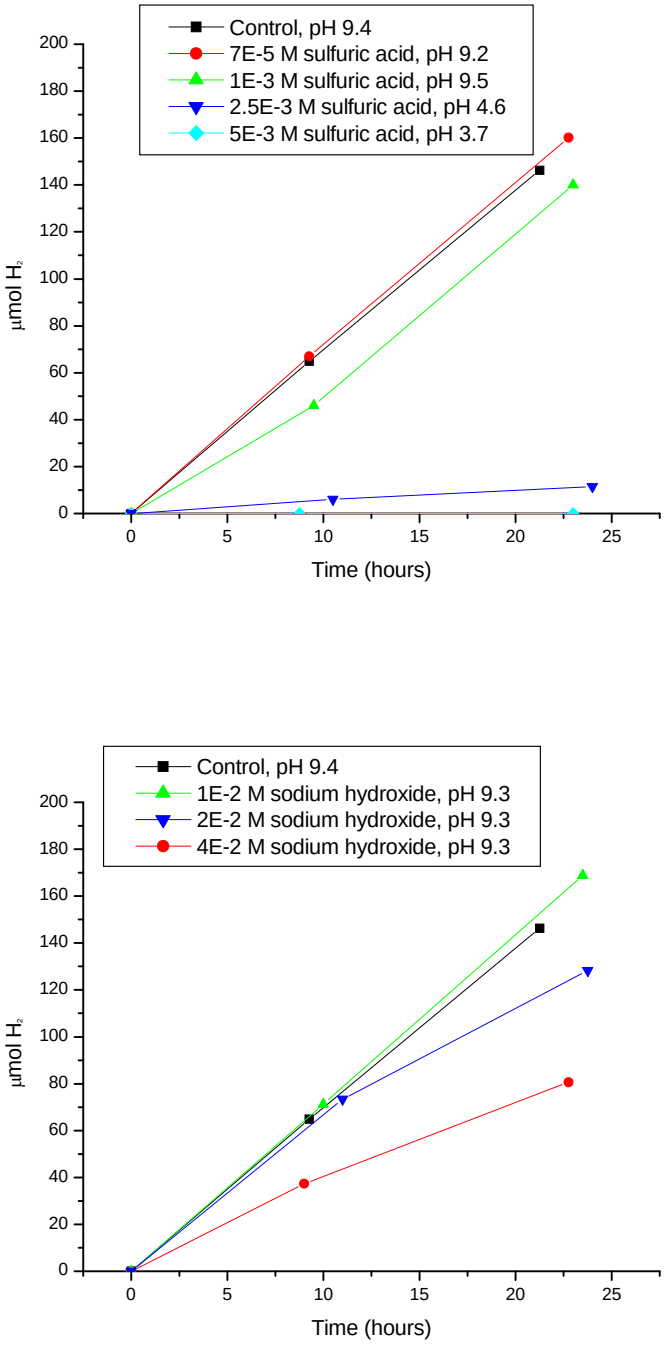

Figure 4.10. Acid concentration (top) and base concentration (bottom) vs. hydrogen production for CdS/Zeolite-Y.

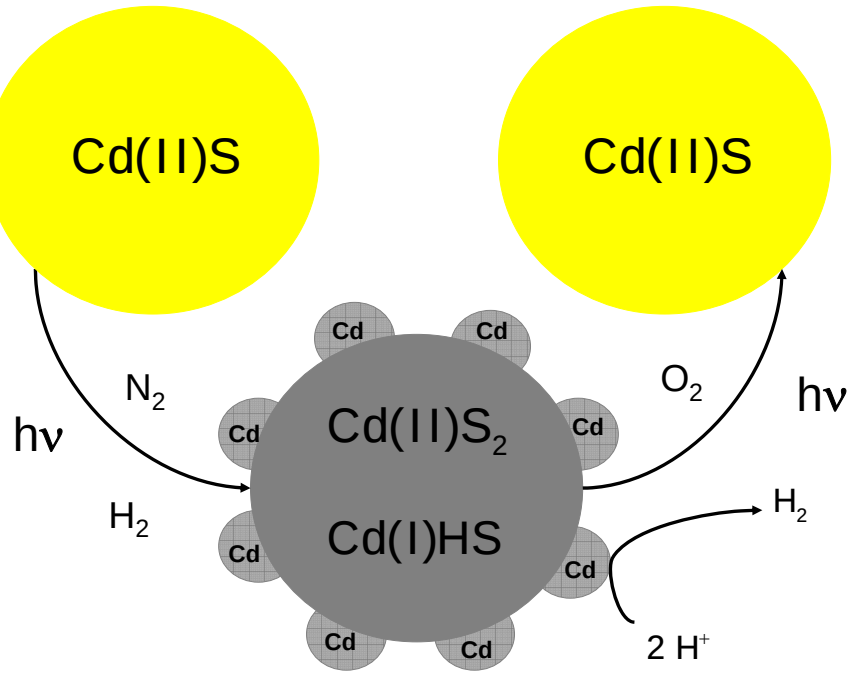

Figure 4.11. Schematic of redox cycling of Cd oxidation state in CdS/zeolite catalysts.

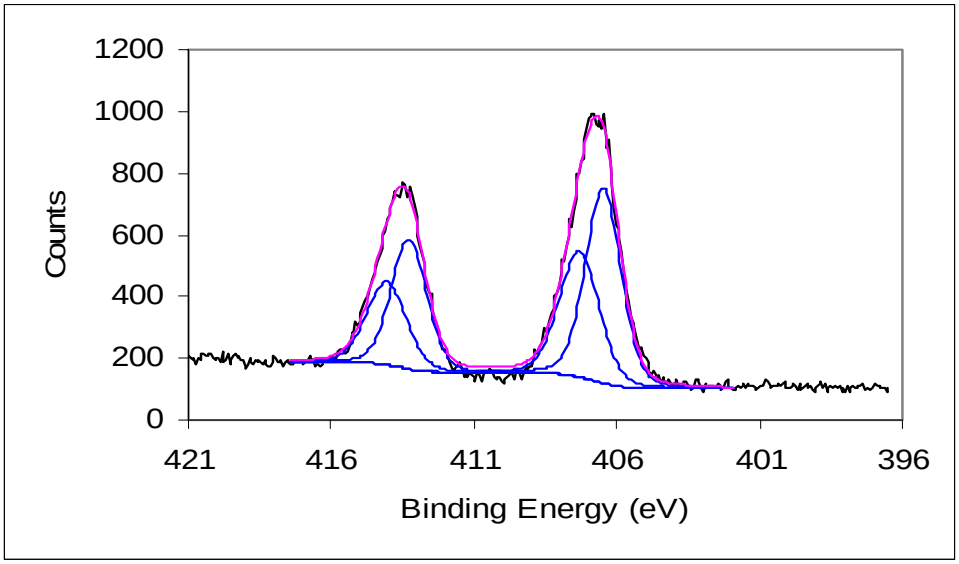

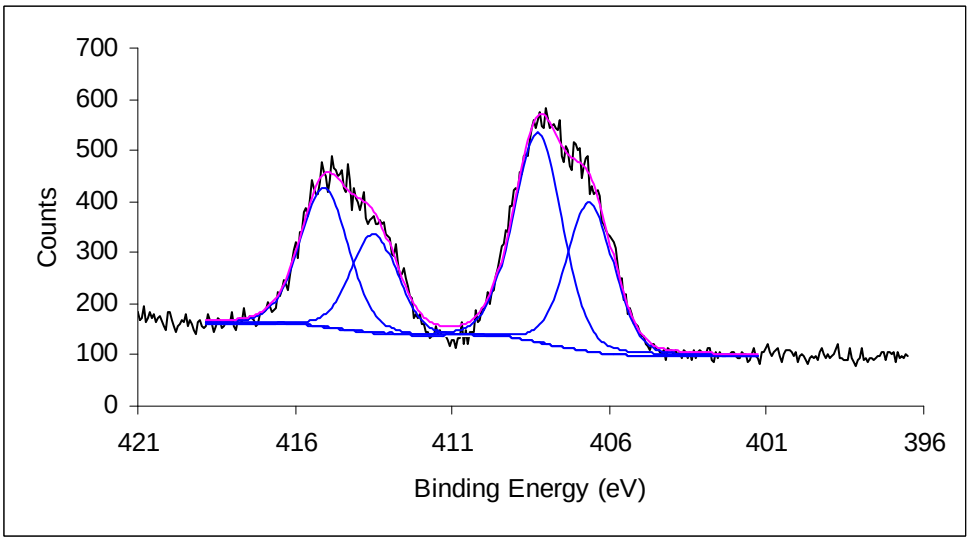

Figure 4.12. XPS of Cd peaks from CdS/Zeolite-Y before (top) and after (bottom) photoreaction.

Material	Bandgap energy (eV)
Commercial CdS	2.29
CdS/NaY	2.31
CdS/zeolite L (small)	2.35
CdS/zeolite L (large)	2.38
CdS/SBA-15	2.44

Table 4.1. Bandgap energies for various CdS/silica composites calculated from Tauc plots.

Material	Surface area (m^2 / g)
NaY zeolite	431
CdS/NaY zeolite	380
Zeolite L (small)	326
Zeolite L (large)	237
CdS/Zeolite L (small)	165
CdS/Zeolite L (large)	122
SBA-15 (calcined)	674
SBA-15 (uncalcined)	435
CdS/SBA-15 (uncal.)	351

Table 4.2. BET surface areas for various CdS/silica composites.

References

(1) Fujishima, A.; Honda, K. *Nature* **1972**, *238*, 37.

(2) Kato, H.; Kudo, A. *J. Phys. Chem. B* **2002**, *106*, 5029.

(3) Ishii, T.; Kato, H.; Kudo, A. *J. Photochem. Photobiol., A* **2004**, *163*, 181.

(4) Tsuji, I.; Kato, H.; Kobayashi, H.; Kudo, A. *J. Am. Chem. Soc.* **2004**, *126*, 13406.

(5) Tsuji, I.; Kato, H.; Kudo, A. *Chem. Mater.* **2006**, *18*, 1969.

(6) Yamasita, D.; Takata, T.; Hara, M.; Kondo, J. N.; Domen, K. *Solid State Ionics* **2004**, *172*, 591.

(7) Niishiro, R.; Kato, H.; Kudo, A. *Phys. Chem. Chem. Phys.* **2005**, *7*, 2241.

(8) Tsuji, I.; Kudo, A. *J. Photochem. Photobiol., A* **2003**, *156*, 249.

(9) Liu, M. Y.; You, W. S.; Lei, Z. B.; Zhou, G. H.; Yang, J. J.; Wu, G. P.; Ma, G. J.; Luan, G. Y.; Takata, T.; Hara, M.; Domen, K.; Can, L. *Chem. Commun.* **2004**, 2192.

(10) Konta, R.; Ishii, T.; Kato, H.; Kudo, A. *J. Phys. Chem. B* **2004**, *108*, 8992.

(11) Tsuji, I.; Kato, H.; Kudo, A. *Angew. Chem. Int. Ed.* **2005**, *44*, 3565.

(12) Zou, Z. G.; Ye, J. H.; Sayama, K.; Arakawa, H. *Nature* **2001**, *414*, 625.

(13) Zou, Z.; Ye, J.; Arakawa, H. *J. Mater. Res.* **2002**, *17*, 1419.

(14) Yin, J. A.; Zou, Z. G.; Ye, J. H. *J. Phys. Chem. B* **2003**, *107*, 61.

(15) Yin, J. A.; Zou, Z. G.; Ye, J. H. *J. Phys. Chem. B* **2003**, *107*, 4936.

(16) Yin, J. A.; Zou, Z. G.; Ye, J. H. *Chem. Phys. Lett.* **2003**, *378*, 24.

(17) Tang, J. W.; Zou, Z. G.; Ye, J. H. *J. Phys. Chem. B* **2003**, *107*, 14265.

(18) Hitoki, G.; Ishikawa, A.; Takata, T.; Kondo, J. N.; Hara, M.; Domen, K. *Chem. Lett.* **2002**, 736.

(19) Kasahara, A.; Nukumizu, K.; Hitoki, G.; Takata, T.; Kondo, J. N.; Hara, M.; Kobayashi, H.; Domen, K. *J. Phys. Chem. A* **2002**, *106*, 6750.

(20) Ishikawa, A.; Takata, T.; Kondo, J. N.; Hara, M.; Kobayashi, H.; Domen, K. *J. Am. Chem. Soc.* **2002**, *124*, 13547.

(21) Kato, H.; Asakura, K.; Kudo, A. *J. Am. Chem. Soc.* **2003**, *125*, 3082.

(22) Shangguan, W. F.; Yoshida, A. *J. Phys. Chem. B* **2002**, *106*, 12227.

(23) Koca, A.; Sahin, M. *Int. J. Hydrog. Energy* **2002**, *27*, 363.

(24) Milczarek, G.; Kasuya, A.; Mamykin, S.; Arai, T.; Shinoda, K.; Tohji, K. *Int. J. Hydrog. Energy* **2003**, *28*, 919.

(25) Roy, A. M.; De, G. C. *J. Photochem. Photobiol. A-Chem.* **2003**, *157*, 87.

(26) Chen, F.; Zhu, Y. P.; Ma, H. L.; Bo, Z. L.; Zhang, J. L. *Acta Phys.-Chim. Sin.* **2004**, *20*, 1292.

(27) Zhang, J. L.; Xiao, M.; Liu, Z. M.; Han, B. X.; Jiang, T.; He, J.; Yang, G. Y. *J. Colloid Interface Sci.* **2004**, *273*, 160.

(28) Innocenti, M.; Cattarin, S.; Loglio, F.; Cecconi, T.; Seravalli, G.; Foresti, M. L. *Electrochim. Acta* **2004**, *49*, 1327.

(29) Yoshimura, J.; Tanaka, A.; Kondo, J. N.; Domen, K. **1995**, *68*, 2439.

(30) Shangguan, W. F.; Yoshida, A. *Sol. Energy Mater. Sol. Cells* **2001**, *69*, 189.

(31) Shangguan, W.; Yoshida, A. *J. Phys. Chem. B* **2002**, *106*, 12227.

(32) Bahnemann, D. W.; Kormann, C.; Hoffmann, M. R. *J. Phys. Chem.* **1987**, *91*, 3789.

(33) Hoffman, A. J.; Carraway, E. R.; Hoffmann, M. R. *Environ. Sci. Technol.* **1994**, *28*, 776.

(34) Hoffman, A. J.; Mills, G.; Yee, H.; Hoffmann, M. R. *J. Phys. Chem.* **1992**, *96*, 5546.

(35) Hoffman, A. J.; Yee, H.; Mills, G.; Hoffmann, M. R. *J. Phys. Chem.* **1992**, *96*, 5540.

(36) Wan, Y.; Williams, C. D.; Duke, C. V. A.; Cox, J. J. *Microporous Mesoporous Mater.* **2001**, *47*, 79.

(37) Ruiz, A. Z.; Li, H. R.; Calzaferri, G. *Angew. Chem. Int. Ed.* **2006**, *45*, 5282.

(38) Zhao, D. Y.; Feng, J. L.; Huo, Q. S.; Melosh, N.; Fredrickson, G. H.; Chmelka, B. F.; Stucky, G. D. *Science* **1998**, *279*, 548.

(39) Davis, A. P.; Huang, C. P. *Water Res.* **1991**, *25*, 1273.

(40) Korgel, B. A.; Monbouquette, H. G. *J. Phys. Chem. B* **1997**, *101*, 5010.

(41) Vucemilovic, M. I.; Vukelic, N.; Rajh, T. . *Photochem. Photobiol., A* **1988**, *42*, 157.

(42) Tang, W. Z.; Huang, C. P. *Water Res.* **1995**, *29*, 745.

(43) Davis, A. P.; Hsieh, Y. H.; Huang, C. P. *Chemosphere* **1994**, *28*, 663.

(44) Hsieh, Y. H.; Huang, C. P.; Davis, A. P. *Chemosphere* **1993**, *27*, 721.

(45) Hsieh, Y. H.; Huang, C. P.; Davis, A. P. *Chemosphere* **1992**, *24*, 281.

(46) Hsieh, Y. H.; Huang, C. P. *Colloids Surf.* **1991**, *53*, 275.

(47) He, Y. J.; Hu, Y. Positron-Annihilation in Cd+2 Ion-Exchanged and Cds Loaded Zeolite-Y. In *Zeolites and Related Microporous Materials: State of the Art 1994*, 1994; Vol. 84; pp 2295.

(48) Li, B. H.; Wang, L. J.; Jin, Q. G.; Guo, Z. Y.; Tang, S. X.; Ding, D. T. *J. Porous Mater.* **2002**, *9*, 287.

(49) Peng, H.; Liu, S. M.; Ma, L.; Lin, Z. J.; Wang, S. J. *J. Cryst. Growth* **2001**, *224*, 274.

(50) Chen, W.; Wang, Z. G.; Lin, L. Y. *J. Lumines.* **1997**, *71*, 151.

(51) Jentys, A.; Grimes, R. W.; Gale, J. D.; Catlow, C. R. A. *J. Phys. Chem.* **1993**, *97*, 13535.

(52) Herron, N.; Wang, Y.; Eddy, M. M.; Stucky, G. D.; Cox, D. E.; Moller, K.; Bein, T. *J. Am. Chem. Soc.* **1989**, *111*, 530.

(53) Wang, Y.; Herron, N. *J. Phys. Chem.* **1988**, *92*, 4988.

(54) Wang, Y.; Herron, N. *J. Phys. Chem.* **1987**, *91*, 257.

(55) Ko, Y. S.; Ahn, W. S. *Bull. Korean Chem. Soc.* **1999**, *20*, 173.

(56) Ko, Y. S.; Ahn, W. S. *Powder Technol.* **2004**, *145*, 10.

(57) Megelski, S.; Calzaferri, G. *Adv. Funct. Mater.* **2001**, *11*, 277.

(58) Ruiz, A. Z.; Bruhwiler, D.; Ban, T.; Calzaferri, G. *Monatsh. Chem.* **2005**, *136*, 77.

(59) Xu, W.; Liao, Y. T.; Akins, D. L. *J. Phys. Chem. B* **2002**, *106*, 11127.

(60) Wang, S.; Choi, D. G.; Yang, S. M. *Adv. Mater.* **2002**, *14*, 1311.

(61) Choi, W. Y.; Termin, A.; Hoffmann, M. R. *Angew. Chem. Int. Ed.* **1994**, *33*, 1091.

(62) Choi, W. Y.; Termin, A.; Hoffmann, M. R. *J. Phys. Chem.* **1994**, *98*, 13669.

(63) Wagner, C. D.; Naumkin, A. V.; Kraut-Vass, A.; Allison, J. W.; Powell, C. J.; Rumble Jr., J. R. NIST X-ray Photoelectron Spectroscopy Database; Measurement Services Division of the National Institute of Standards and Technology, 2006.